# Generation of Alfvén Waves by Magnetic Reconnection

#### Hiromitsu Kigure

hiromitu@kusastro.kyoto-u.ac.jp

Kwasan and Hida Observatories, Kyoto University, Yamashina, Kyoto 607-8471

# Kunio Takahashi

kutaka@jmastec.go.jp

Research Institute for Global Change, JAMSTEC, 3173-25 Showa-machi, Kanazawaku, Yokohama, Kanagawa 236-0001

#### Kazunari Shibata

Kwasan and Hida Observatories, Kyoto University, Yamashina, Kyoto 607-8471 Takaaki Yokoyama

Department of Earth and Planetary Science, University of Tokyo, 7-3-1 Hongo, Bunkyo-ku, Tokyo 113-0033

and

# Satoshi Nozawa

Department of Science, Ibaraki University, Bunkyo 2-1-1 Mito, Ibaraki 310-8512

(Received; accepted)

#### Abstract

In this paper, results of 2.5-dimensional magnetohydrodynamical simulations are reported for the magnetic reconnection of non-perfectly antiparallel magnetic fields. The magnetic field has a component perpendicular to the computational plane, that is, guide field. The angle  $\theta$  between magnetic field lines in two half regions is a key parameter in our simulations whereas the initial distribution of the plasma is assumed to be simple; density and pressure are uniform except for the current sheet region. Alfvén waves are generated at the reconnection point and propagate along the reconnected field line. The energy fluxes of the Alfvén waves and magnetoacoustic waves (slow mode and fast mode) generated by the magnetic reconnection are measured. Each flux shows the similar time evolution independent of  $\theta$ . The percentage of the energies (time integral of energy fluxes) carried by the Alfvén waves and magneto-acoustic waves to the released magnetic energy are calculated. The Alfvén waves carry 38.9%, 36.0%, and 29.5% of the released magnetic energy at the maximum ( $\theta = 80^{\circ}$ ) in the case of  $\beta = 0.1$ , 1, and 20 respectively, where  $\beta$  is the plasma  $\beta$  (the ratio of gas pressure to magnetic pressure). The magneto-acoustic waves carry  $16.2\% (\theta = 70^{\circ}), 25.9\% (\theta = 60^{\circ}), \text{ and } 75.0\% (\theta = 180^{\circ}) \text{ of the energy at}$ the maximum. Implications of these results for solar coronal heating and acceleration

of high-speed solar wind are discussed.

Key words: MHD — Sun: corona — Sun: magnetic fields — waves

## 1. Introduction

The heating mechanism of the solar corona is one of the most mysterious issue in astrophysics (Aschwanden 2004). The structure of the solar atmosphere consists of the photosphere, the temperature of which is about or more than six thousand degrees, the chromosphere, the temperature of which is up to a few ten thousand degrees, the transition region, in which the temperature increases rapidly, and the corona, the temperature of which reaches a few million degrees. To maintain such a high temperature in the corona in spite of cooling by heat conduction and radiative losses, a continuous supply of thermal energy is necessary.

X-ray observations from early space experiments (e.g., Skylab) have shown that the corona is not uniform and consists of many bright loops. Poletto et al. (1975) demonstrated a correspondence between enhanced X-ray emission and a magnetic loop. It is therefore suggested that magnetic activity is related to the heating of the solar corona. Related to the magnetic activity, there are two promising models for coronal heating (see reviews by Klimchuk 2006, Erdélyi & Ballai 2007 and also references therein). One is heating by the dissipation of Alfvén waves <sup>1</sup> that propagate in the magnetic flux tubes (Alfvén 1947; Hollweg 1973, 1981, 1984, 1986; Uchida & Kaburaki 1974; Wentzel 1974; McKenzie, Banaszkiewicz, & Axford 1995; Axford et al. 1999). There are many proposed mechanisms for the dissipation of Alfvén waves, such as mode conversion (see the next paragraph), resonant absorption (e.g., Ionson 1978; Poedts et al. 1989; Erdélyi & Goossens 1995; Ruderman et al. 1997), phase mixing (e.g., Heyvaerts & Priest 1983), or magnetohydrodynamic (MHD) turbulence (e.g., Inverarity & Priest 1995; Matthaeus et al. 1999). The other is heating by many small-scale flares, i.e., nanoflares triggered by magnetic reconnection (Parker 1988). Observationally the occurrence frequency of microflares and nanoflares, N, has been found to be  $dN/dW \propto W^{-\alpha}$ , where W is the total flare energy. The power-law index, α, ranges from 1.5 to 1.8 (Hudson 1991; Shimizu 1995; Shimojo & Shibata 1999; Aschwanden & Parnell 2002) and nanoflares can not account for coronal heating if  $\alpha$  is less than 2. However, a value of  $\alpha$  larger than 2 has also been found (Krucker & Benz 1998; Parnell & Jupp 2000). The definitive conclusion has not yet been obtained from observations.

As an origin of Alfvén waves, Kudoh & Shibata (1999) considered a photospheric random motion propagating along an open magnetic flux tube in the solar atomosphere, and performed 1.5-dimensional (1.5D, i.e., torsional motion is allowed) MHD simulations for solar spicule formation and the heating of the corona. It was shown that Alfvén waves transport sufficient

Other types of waves (acoustic, slow-mode and fast-mode waves) are strongly damped or reflected at the steep density and temperature gradients of chromosphere and transition region.

energy flux into the corona to account for its heating, by extending the work by Hollweg, Jackson, & Galloway (1982) (see also Saito, Kudoh, & Shibata 2001). Moriyasu et al. (2004) performed 1.5D MHD simulations of the propagation of nonlinear Alfvén waves along a closed magnetic loop including heat conduction and radiative cooling. They found that the corona is episodically heated by fast- and slow-mode MHD shocks generated by nonlinear Alfvén waves via nonlinear mode-coupling. It was also found that the time variation of the simulated extreme-ultraviolet (EUV) and X-ray intensities is quite similar to the observed one. They concluded that the observed nanoflares may not be a result of reconnection but may be due to nonlinear Alfvén waves. Subsequently, Antolin et al. (2008) discussed the observational signatures of the power-law indexes and coronal heating mechanisms (Alfvén waves and nanoflares) by using 1.5D MHD model of Moriyasu et al. (2004). They found that Alfvén heating and nanoflare heating exhibit different power-law indexes (see also Antolin & Shibata 2010).

However, since Alfvén waves can be generated by magnetic reconnection unless the reconnection takes place in perfectly antiparallel magnetic fields, the nanoflare model may not be very different from the Alfvén wave model. Yokoyama & Shibata (1995) modelled jets (X-ray or EUV jets and serges observed with H $\alpha$  in the chromosphere) by performing a resistive two-dimensional MHD simulation of the magnetic reconnection occurring in the current sheet between emerging magnetic flux and overlying pre-existing coronal magnetic fields. Recent Hinode (Kosugi et al. 2007) observation revealed that jets are ubiquitous in the chromosphere (Shibata et al. 2007). Nishizuka et al. (2008) proved that the jets on the basis of this model are quantitatively corresponding to the multiwavelength jets (see also Cirtain et al. 2007 and Liu et al. 2009) observed with Hinode and TRACE (Handy et al. 1999). Yokoyama (1998) found that the ratio of energy of Alfvén waves to the energy released by the magnetic reconnection (the model of Yokoyama & Shibata 1995) is nearly equal to 3%. In this model, there is a shear between emerging magnetic fields and coronal magnetic fields, kinks are produced by the magnetic reconnection and propagate away as Alfvén waves.

Takeuchi & Shibata (2001) performed 2.5-dimensional (2.5D) MHD simulations of the photospheric magnetic reconnection caused by convection, and found that the energy flux of Alfvén waves <sup>2</sup> is enough to explain both coronal heating and spicule production. The generation of Alfvén waves through magnetic reconnection has been also discussed by Parker (1991), Axford et al. (1999), and Sturrock (1999) in the context of coronal hole heating and solar wind acceleration.

The upward acoustic waves in the flux tube are expected to be transported as other waves (e.g., slow-mode waves) after the formation of the shocks. Slow-mode waves are also thought to contribute to coronal heating though the contribution is only to the relatively low corona because of their compressibility. Takeuchi & Shibata (2001) measured the energy flux of slow-mode waves and found that it was ten times larger than that of Alfvén waves. Suzuki

<sup>&</sup>lt;sup>2</sup> The perpendicular magnetic field injected by magnetic reconnection propagates as Alfvén waves.

(2002) discussed the possibility of coronal heating and the acceleration of the low-speed solar wind by slow-mode waves. Suzuki (2004) developed his study by including fast-mode waves (linearly polarized Alfvén waves) and showed that slow-mode waves contribute to the heating of the low corona and the acceleration of the low-speed solar wind, while linearly polarized Alfvén waves contribute to the heating of the outer corona and the acceleration of the high-speed solar wind.

As the mention above, waves are created by torsional motions as recently observed (e.g., Bonet et al. 2008) in the photosphere or magnetic reconnections. They propagate into the corona and disipate their energy through linear and non-linear mechanisms. In particular, Alfvén waves can be generated by such drivers, for the first time, by Jess et al. (2009). From Hinode data, De Pontieu et al. (2007) estimated the energy flux carried by transversal oscillations generated by spicules and compared with radiative MHD simulations by more realistically extending Kudoh & Shibata (1999). They indicated that the calculated energy flux is enough to heat the quiet corona and to accelerate the high-speed solar wind. Okamoto et al. (2007) also estimated the energy flux to be  $2 \times 10^6$  ergs cm<sup>-2</sup> s<sup>-1</sup> propagating on coronal magnetic fields. These reports (see also Tomczyk et al. 2007), however, have considerable argument about what is Alfvén waves. Erdélyi and Fedun (2007) and Van Doorsselaere et al. (2008) argued that these oscillations were likely to be kink oscillations from observed behavior (see also Goossens et al. 2009; Taroyan & Erdélyi 2009).

It is thought that the magnetic reconnection causes the solar flare. Particle acceleration takes place associated with solar flare. The mechanism of the particle acceleration, however, is not made clear. Alfvén waves could contribute to the acceleration of ions through cyclotron resonance (see, e.g., Miller 2000, and references therein). The generation of Alfvén waves by the magnetic reconnection is a very interesting research topic also from such a point of view.

In this paper, we present the results of 2.5D MHD simulations of the Alfvén wave generation by the reconnection of non-perfectly antiparallel magnetic fields. The initial magnetic fields have a shear, i.e., the magnetic field has a component perpendicular to the computational plane. This component can not contribute to the reconnection and is so-called guide field. The magnetic reconnection in this geometry was analytically studied by Petschek & Thorne (1967). The angle between the magnetic field lines in two half regions is a parameter,  $\theta$ , while the initial distribution of the plasma is assumed to be simple. The energy fluxes of Alfvén waves and magneto-acoustic waves are measured. In section 2 we describe the numerical method and model. In section 3 we show the results of the simulations. Finally a discussion and summary are given in section 4.

#### 2. Numerical Simulations

# 2.1. Assumptions and Basic Equations

In this paper, we assume that the distributions of the physical quantities are not dependent on the z-coordinate but that the vector fields have the z-component (i.e., 2.5D approximation). We solve the following resistive MHD equations numerically:

$$\frac{\partial \rho}{\partial t} + (\boldsymbol{v} \cdot \nabla)\rho = -\rho(\nabla \cdot \boldsymbol{v}),\tag{1}$$

$$\frac{\partial \boldsymbol{v}}{\partial t} + (\boldsymbol{v} \cdot \nabla) \boldsymbol{v} = -\frac{1}{\rho} \nabla p + \frac{1}{4\pi\rho} (\boldsymbol{j} \times \boldsymbol{B}), \qquad (2)$$

$$\frac{\partial p}{\partial t} + (\boldsymbol{v} \cdot \nabla)p = -\gamma p(\nabla \cdot \boldsymbol{v}) + (\gamma - 1)\frac{\eta}{4\pi} |\boldsymbol{j}|^2, \tag{3}$$

$$\frac{\partial \boldsymbol{B}}{\partial t} = -\nabla \times \boldsymbol{E},\tag{4}$$

$$\boldsymbol{E} = \eta \boldsymbol{j} - \boldsymbol{v} \times \boldsymbol{B},\tag{5}$$

and

$$j = \nabla \times \boldsymbol{B},\tag{6}$$

where  $\rho, p, v$  are the density, pressure, and velocity of the gas, B, E, j are the magnetic field, electric field, and current density, and  $\gamma$ ,  $\eta$  represent the ratio of specific heats and electric resistivity.

## 2.2. Initial Conditions and Boundary Conditions

We consider the situation that the physical quantities are uniform far from the current sheet. Their typical quantities are  $\rho_0 = 1$ ,  $p_0 = 1/\gamma$ , and  $B_0 = |\mathbf{B}_0| = \sqrt{8\pi/(\beta\gamma)}$ , where  $\mathbf{B}_0$  is the initial magnetic field.  $\beta = 8\pi p_0/B_0^2$  is the plasma  $\beta$  (the ratio of gas pressure to magnetic pressure). Initially the magnetic pressure gradient force balances with the gas pressure gradient force. The sound speed,  $C_S = \sqrt{\gamma p/\rho}$ , is unity in the whole domain of the simulation box.

The initial distributions of the physical quantities are as follows:

$$B_y = B_0 \tanh\left(2\frac{x}{L_0}\right) \cos\phi,\tag{7}$$

$$B_z = B_0 \tanh \left| 2\frac{x}{L_0} \right| \sin \phi, \tag{8}$$

$$B_x = v_x = v_y = v_z = 0, (9)$$

$$p = p_0 \left( 1 + \frac{1}{\beta} \right) - \frac{B_y^2 + B_z^2}{8\pi},\tag{10}$$

and

$$\rho = \gamma p,\tag{11}$$

where

$$\phi = 90^{\circ} - \frac{\theta}{2},\tag{12}$$

 $L_0$  is the thickness of the initial current sheet. In this study, we have adopted  $\gamma = 5/3$  and  $L_0 = 1$ .

Figure 1 shows the coordinate system (xy-plane and yz-plane), the initial magnetic field configuration, and the definition of  $\theta$  and  $\phi$  (the directions of the wave vector and  $B_{\perp}$  discussed in section 3.1 are also displayed). When  $\theta$  is equal to 180° the magnetic fields are perfectly antiparallel on both sides of a line where x=0. We investigated the cases where  $\theta$  is from 180° to 10°. The value of the plasma  $\beta$  is also a variable parameter and equal to 0.1, 1, or 20. All physical quantities are normalized by their typical values. This means that the velocity is normalized by the initial sound speed,  $C_{\rm S0} = \sqrt{\gamma p_0/\rho_0}$ . Time is normalized by  $t_0 = L_0/C_{\rm S0}$ .

The number of grid points in the simulations is  $603 \times 1003$ . The grid spacing is uniform within  $-5L_0 \le x \le 5L_0$  and  $-20L_0 \le y \le 20L_0$ . The constant grid spacing in the x-direction is equal to  $0.025L_0$  and that in the y-direction is  $0.05L_0$ . The grid spacing in the non-uniform region is slowly stretched by an increment of 2 % at each grid step (e.g.,  $|\Delta x_{i+1}| = 1.02|\Delta x_i|$ ). The size of the computational domain is  $-13.1L_0 \le x \le 13.1L_0$ ,  $-36.3L_0 \le y \le 36.3L_0$ .

At all the boundaries of the simulation box the periodic boundary condition is assumed. The total energy is therefore conserved. It can be said that the decrease of the magnetic energy in the simulation box is equal to the energy released by the magnetic reconnection.

## 2.3. Resistivity Model and Numerical Method

In order to initiate the magnetic reconnection, we assume a localized resistivity near the origin, (x,y) = (0,0), as

$$\eta = \begin{cases}
\eta_0 \left[ 2 \left( r/r_{\eta} \right)^3 - 3 \left( r/r_{\eta} \right)^2 + 1 \right], & (r \le r_{\eta}), \\
0, & (r > r_{\eta}),
\end{cases}$$
(13)

where  $r = (x^2 + y^2)^{1/2}$ ,  $r_{\eta} = L_0$ , and  $\eta_0 = 0.1C_{\rm S0}L_0$ . The magnetic Reynolds number is  $R_{\rm m} \equiv v_{\rm A0}L_y/\eta_0$ , where  $v_{\rm A0}$  is the initial Alfvén velocity outside the current sheet and  $L_y (= y_{\rm max} - y_{\rm min} = 72.6L_0)$  is the size of the computational domain in the y-direction. The values of the plasma  $\beta$  and  $R_{\rm m}$  in our simulations are summarized in Table 1. We here mention that this non-dimensional parameter,  $R_{\rm m}$ , is much smaller than that of typical solar corona plasma  $(R_{\rm m} \sim 10^{14})$ . However the numerical treatment of  $R_{\rm m} \sim 10^{14}$  is very difficult in current-day computer resources.

The numerical computations were carried out by the Rational CIP (Cubic interpolated profile) method (Yabe & Aoki 1991; Xiao, Yabe & Ito 1996) combined with the MOC-CT method (Evans & Hawley 1988; Stone & Norman 1992). The magnetic induction equation was solved by the MOC-CT and the other equations were solved by the CIP (e.g., Kudoh, Matsumoto & Shibata 1998; Kigure & Shibata 2005; Takahashi et al. 2009).

#### 3. Results of Numerical Simulations

# 3.1. Time Evolution

First we describe the time evolution of the system only in the case of plasma  $\beta = 0.1$ . Figures 2a and 2b show the distribution of the logarithmic pressure in the case of  $\theta = 180^{\circ}$ . The magnetic fields reconnect in the diffusion region, which is around (x,y) = (0,0) and the magnetic energy is converted to thermal energy. The plasma is accelerated in the y-direction by the magnetic tension of the reconnected magnetic field. The diffusion region is localized so that the Petschek-type reconnection takes place. The slow-mode MHD shock is therefore formed, i.e., the gas pressure increases and the magnetic pressure decreases behind the shock front. The velocity of the reconnection outflow is the order of Alfvén velocity. These are equivalent to the magnetic energy being converted to thermal and kinetic energy through the shock front.

Figures 2c and 2d show the distribution in the case of  $\theta = 140^{\circ}$  and  $\theta = 90^{\circ}$ . The y-components of the initial magnetic field in these cases are less than that in the  $\theta = 180^{\circ}$  case (the difference in the number of the contour indicates this situation) while the z-components are not equal to zero in these cases. Figure 3 shows the distribution of the x-component of the velocity normalized by  $v_{A0}\cos(90^{\circ} - \theta/2) = v_{A0,eff}$  on a line where y = 0 at  $t/t_0 = 20$ . The triangles display the results of the  $\theta = 180^{\circ}$  case, the squares display the results of the  $\theta = 140^{\circ}$  case, and the plus signs the  $\theta = 90^{\circ}$  case. The inflow velocities  $v_{in}$ , especially near the current sheet  $(|x|/L_0 < 2)$ , are proportional to  $v_{A0,eff}$ .

From the linearized MHD equations, the disturbance of velocity and magnetic field due to the Alfvén wave is perpendicular to the initial (non-perturbed) magnetic field,  $\mathbf{B}_0$ , and the wave vector,  $\mathbf{k}$  (i.e., parallel to  $\mathbf{k} \times \mathbf{B}_0$ ). In our case, the initial magnetic field is on the yz-plane. For simplicity, we assume that the wave vector is approximated to be parallel to the x (or -x) direction (the Alfvén wave front is on the yz-plane). In this case, the perturbed components of velocity and magnetic field are on the yz-plane (no x-component) and perpendicular to the initial field. Hereafter, we call these velocity and magnetic field disturbances due to the Alfvén wave as  $v_{\perp}$  and  $B_{\perp}$ . In this case, the perturbed components are described as  $v_{\perp} = v_y \sin \phi - v_z \cos \phi$  and  $B_{\perp} = B_y \sin \phi - B_z \cos \phi$  (see Figure 1). Note that the non-linear effect of shock propagating through the magnetic reconnection is included. However, it is difficult to remove the non-linear effect from these components. Therefore, this assumption would be acceptable for our first attempt to study the magnetic disturbance of non-perfectly antiparallel magnetic reconnection.

In the case where there exists a magnetic field component perpendicular to the xyplane, the field component perpendicular to the initial field,  $B_{\perp}$ , is generated as a result of
the reconnection although  $B_{\perp}$  is not generated in the perfectly antiparallel reconnection (in the
perfectly antiparallel reconnection case,  $B_{\perp}$  means  $B_z$ ). The generated  $B_{\perp}$  propagates as Alfvén
waves along field lines. The left four panels of Figures 4 and 5 show the time evolutions of  $-B_{\perp}$ 

in the cases of  $\theta = 140^{\circ}$  and  $\theta = 90^{\circ}$  respectively. The contour lines show the magnetic field lines and the arrows show the velocity. The right panels of Figures 4 and 5 show the  $B_z$  distribution at  $t/t_0 = 25$ . Following a certain magnetic field line, e.g., from the point  $(x/L_0, y/L_0) = (-3, 20)$  in the  $\theta = 140^{\circ}$  case,  $B_z$  once increases and then decreases with keeping its sign. This feature is consistent with the analytical solution in Petschek & Thorne (1967) (see Figure 3 in that paper). The point where  $B_z$  increases corresponds to Alfvén wave and the point where  $B_z$  decreases corresponds to slow-mode MHD shock.

# 3.2. Energy Fluxes of Alfvén Waves and Magneto-acoustic Waves

In this study, we focus on the disturbance energy fluxes carried by the Alfvén waves  $(F_{\text{Alfven}})$  and magneto-acoustic waves  $(F_{\text{Sound}})$  generated by the magnetic reconnection. These fluxes are measured on a line where  $y/L_0 = \pm 10$ .

$$F_{\text{Alfven}} = \pm \frac{1}{4\pi L_x} \int_{x_{\text{min}}}^{x_{\text{max}}} -B_{\perp} v_{\perp} B_{\parallel y} \ dx, \tag{14}$$

$$F_{\text{Sound}} = \pm \frac{1}{L_x} \int_{x_{\min}}^{x_{\max}} \delta p \ v_{\parallel y} \ dx, \tag{15}$$

where  $\delta$  means the difference from the initial value,  $L_x(=x_{\text{max}}-x_{\text{min}}=26.2L_0)$  is the size of the computational domain in the x-direction.  $v_{\parallel y}$  ( $B_{\parallel y}$ ) is the y-component of velocity (magnetic field) parallel to the initial magnetic field,  $\mathbf{B}_0$ .  $v_{\parallel y}$  and  $B_{\parallel y}$  are described as

$$v_{\parallel y} = \frac{v_y B_{y0}^2 + v_z B_{y0} B_{z0}}{B_{y0}^2 + B_{z0}^2},\tag{16}$$

$$B_{\parallel y} = \frac{B_y B_{y0}^2 + B_z B_{y0} B_{z0}}{B_{y0}^2 + B_{z0}^2}.$$
 (17)

Here,  $B_{y0}$  ( $B_{z0}$ ) is the y(z)-component of the initial magnetic field. The plus sign is on the  $y/L_0 = 10$  line and the minus sign on the  $y/L_0 = -10$  line. We also measure the time integral of each flux:

$$E_{\text{Alfven}} = L_x \int_0^t F_{\text{Alfven}} dt, \tag{18}$$

$$E_{\text{Sound}} = L_x \int_0^t F_{\text{Sound}} dt. \tag{19}$$

 $F_{\text{Alfven}}$  and  $F_{\text{Sound}}$  are normalized by  $\rho_0 C_{\text{S0}}^3$ .  $E_{\text{Alfven}}$  and  $E_{\text{Sound}}$  are normalized by  $\rho_0 C_{\text{S0}}^2 L_0^2$ . The origin of the energies transported by the Alfvén waves and magneto-acoustic waves is the magnetic energy released by the reconnection so that the magnetic energy in the simulation domain is also measured.

Figures 6a-c show the time evolutions of the released magnetic energy ( $\Delta E_{\rm mg} \equiv E_{\rm mg0} - E_{\rm mg}$ ) in the simulation domain, where  $E_{\rm mg}$  is defined by

$$E_{\rm mg} = \frac{1}{8\pi} \int_{x_{\rm min}}^{x_{\rm max}} \int_{y_{\rm min}}^{y_{\rm max}} |\mathbf{B}|^2 dx dy, \tag{20}$$

and  $E_{\rm mg}$  is normalized by  $\rho_0 C_{\rm S0}^2 L_0^2$ . Here,  $E_{\rm mg0}$  is the initial magnetic energy in the simulation

domain. It is clear that the amount of the released magnetic energy decreases as the angle of magnetic shear,  $\theta$ , decreases and the plasma  $\beta$  increases. In the final evolutional stage of each calculation, the magnetic energy in the simulation domain decreases linearly with time. Figure 6d shows the value of  $|dE_{\rm mg}/dt|$  in the case of  $\theta = 180^{\circ}, 140^{\circ}$  and 90°. The magnetic energy released by the magnetic reconnection is equivalent to the Poynting flux entering into the reconnection region. Since the reconnection inflow,  $v_{\rm in}$ , is expressed as  $v_{\rm in} = \epsilon v_{\rm A} \propto B$  in the case of Petschek-type reconnection, where  $\epsilon$  is the reconnection rate and roughly independent of B (e.g., Magara et al. 1996, Yokoyama & Shibata 1997),

$$-\frac{dE_{\rm mg}}{dt} \sim 2\frac{B^2}{4\pi} l v_{\rm in} \propto B^3 \propto \beta^{-3/2},\tag{21}$$

where l is the size of reconnection region (Tanuma et al. 1999). The solid line in Figure 6d shows a line where  $|dE_{\rm mg}/dt| \propto \beta^{-3/2}$ . It is clear from Figure 6d that the Equation (21) is almost satisfied independent of  $\theta$ .

Figures 7a and 7b show the time evolutions of the energy fluxes carried by the Alfvén waves and magneto-acoustic waves,  $F_{\text{Alfven}}$  and  $F_{\text{Sound}}$ , in the case of  $\beta = 0.1$ . If  $\theta = 180^{\circ}$ ,  $F_{\text{Alfven}}$  is always zero because the perturbation perpendicular to the initial field is not generated. The time evolutions of the magneto-acoustic wave flux are similar in each case except when  $\theta \leq 60^{\circ}$ . Those of the Alfvén wave flux are also similar except for the cases where  $\theta = 180^{\circ}$  and  $\theta \leq 60^{\circ}$ . The magneto-acoustic and Alfvén wave fluxes decrease after reaching the peak value.

Figure 7c and 7d are the case of  $\beta=1$ . The time evolutions of  $F_{\text{Alfven}}$  and  $F_{\text{Sound}}$  in this case are similar in each  $\theta$  case respectively and similar to those in the  $\beta=0.1$  case. There is a following tendency;  $F_{\text{Alfven}}$  at the late stage once increases and then decreases as  $\theta$  decreases, while  $F_{\text{Sound}}$  at the late stage decreases monotonically. Figures 7e and 7f show the results for the case of  $\beta=20$ . Though the same features are seen,  $F_{\text{Alfven}}$  and  $F_{\text{Sound}}$  are different by more than one order of magnitude when compared with the  $\beta=1$  case (the time at the late stage of the  $\beta=20$  case is about 3.5 times larger than that of the  $\beta=1$  case, i.e., the time integral is made about 3.5 times longer).

### 4. Discussions and Summary

Figure 8 shows the ratio (percentage) of the energies carried by the Alfvén waves and magneto-acoustic waves ( $E_{\text{Alfven}}$  and  $E_{\text{Sound}}$ ) to the released magnetic energy at the final stage of simulation. In the case of  $\theta = 180^{\circ}$ ,  $E_{\text{Alfven}}$  is equal to 0 independent of the plasma  $\beta$  because the magnetic field component perpendicular to the initial field is not generated by the reconnection. As  $\theta$  decreases the percentage of the energy carried by the Alfvén waves increases up to 38.9%, 36.0%, and 29.5% in the case of  $\beta = 0.1$ , 1, and 20 respectively, and then decreases. The percentage is maximum when  $\theta = 80^{\circ}$ . The percentage of the energy carried by the magneto-acoustic waves is roughly constant when  $\theta$  is relatively large in the cases of  $\beta = 0.1$  and 1. In the case of  $\beta = 20$ , it gradually decreases in decreasing  $\theta$ . The maximum values are

16.2%, 25.9%, and 75.0% in the case of  $\beta = 0.1$ , 1, and 20 respectively.

While the percentage of the energy carried by the Alfvén waves is almost independent of  $\beta$ , that of the energy carried by the magneto-acoustic waves changes by some factor. The ratio of the energy carried by the magneto-acoustic waves to the released magnetic energy becomes larger as  $\beta$  becomes larger in  $\theta \geq 40$ . This means that the significant part of the energy released by the magnetic reconnection is transported as a perturbation of gas pressure in a high- $\beta$  plasma case.

This result can give a suggestion to the study of high- $\beta$  plasma astrophysical objects, e.g., the accretion disk. The accretion disk is thought to be weakly magnetized. The magnetic reconnection is induced by the magnetorotational instability (e.g., Sano & Inutsuka 2001, Machida & Matsumoto 2003). Sano & Inutsuka (2001) showed that the heating rate is strongly related to the turbulent shear stress, which determines the efficiency of angular momentum transport. Therefore, the study of the magnetic reconnection in a high- $\beta$  plasma is important.

The total non-radiative energy input to the solar coronal hole was estimated at  $5 \times 10^5$  ergs cm<sup>-2</sup> s<sup>-1</sup> by Withbroe (1988). For the acceleration of high-speed solar wind, some  $1 \times 10^5$  ergs cm<sup>-2</sup> s<sup>-1</sup> is required to be deposited at distances of several solar radii (see, e.g., Parker 1991, and references therein). If the solar wind is accelerated by the energy flux of Alfvén waves, this means that 20% of the energy released by reconnection events in the solar corona is transferred as a form of Alfvén wave. Our results show that the energy larger than the required can be carried by the Alfvén wave independent of  $\beta$  around the parametric region of  $60^{\circ} \le \theta \le 110^{\circ}$ . These energies are converted to thermal energy through the dissipation of Alfvén waves.

The guide field,  $B_z$  in this paper, can not contribute to the reconnection because of the 2.5D approximation. Besides this, the reconnection progresses typically with the Alfvén time scale, which depends on the magnetic field on the xy-plane (more exactly speaking, depend on the reconnection component of the Alfvén velocity). It is therefore interesting that how the results change when the normalizations are changed: Time is re-normalized by the effective Alfvén time ( $t_{A0,eff} = L_0/v_{A0,eff}$ ). This means that the same time in Figure 6 is not the same time in Figure 9 because the effective Alfvén velocity is different according to  $\theta$ . The magnetic field is also re-normalized by the initial magnetic field which can reconnect ( $B_0 \sin \theta/2$ ). When  $\theta = 0$ , the magnetic field is uniform and the reconnection does not take place.

Figure 9 shows the difference of the re-normalized magnetic energy from the initial value as the function of re-normalized time in each  $\theta$  case. In the high- $\beta$  case, the magnetic energy is released at almost the same rate in the effective Alfvén time when  $\theta \geq 40^{\circ}$ . The lower  $\beta$  is, the larger the discrepancy of the release rate becomes. Figure 10 shows the re-normalized energy fluxes and the time integral of those as the function of re-normalized time. The energy flux and its time integral of Alfvén waves show the time variation similar to each other independent of  $\beta$ . Those of magneto-acoustic waves also show the time variation similar to each other except

when  $\theta$  is relatively small, although there is a bit of  $\beta$  dependence. Compared with Figure 7, the peak positions are matched.

Figure 11 indicates the percentage of the energies carried by the Alfvén waves and magneto-acoustic waves to the released magnetic energy. The vertical axis is re-normalized as same as the above-mentioned way. This shows clearly that the amount of the energy carried by the Alfvén waves has almost the same dependence on  $\theta$  independent of  $\beta$  if the energy and time are scaled by the effective magnetic energy and Alfvén time. This is equivalent to that the magnetic configuration is important rather than the field strength relative to the gas pressure for the energy release rate in the effective Alfvén time. On the other hand, the amount of the energy carried by the magneto-acoustic waves shows the  $\beta$  dependence.

In this paper, we have reported the results for 2.5D MHD simulations of the magnetic reconnection. When magnetic fields are non-perfectly antiparallel, the magnetic field component perpendicular to the initial field is generated and propagates as the Alfvén wave. We have measured the energy fluxes of Alfvén waves and magneto-acoustic waves. Magneto-acoustic waves are related to fast mode waves in the high- $\beta$  case ( $\beta = 20$ ) and slow mode waves in the low- $\beta$  case ( $\beta = 0.1$ ). The energy carried by the Alfvén waves is more than 30% of the energy released by the magnetic reconnection at the maximum. That value satisfies the requirement for energy flux of Alfvén waves necessary for acceleration of high-speed solar wind in the nanoflare coronal heating model. For more exact discussion, 3-dimensional simulations with more realistic plasma distribution are necessary.

We would like to thank David H. Brooks and Takeru Suzuki for helpful comments. This study was initiated as a part of the ACT-JST summer school for numerical simulations in astrophysics and in space plasmas. Numerical computations were carried out on VPP5000 (project ID: yhk32b, rhk05b, and whk08b) and the general-purpose PC farm (project P.I. KT) at Center for Computational Astrophysics, CfCA, of National Astronomical Observatory of Japan. This work was supported by the Grant-in-Aid for the 21st Century COE "Center for Diversity and Universality in Physics" from the Ministry of Education, Culture, Sports, Science and Technology (MEXT) of Japan.

## References

Alfvén, H. 1947, MNRAS, 107, 211

Antolin, P., Shibata, K., Kudoh, T., Shiota, D., & Brooks, D. 2008, ApJ, 688, 669

Antolin, P., & Shibata, K. 2010, ApJ, 712, 494

Aschwanden, M. J., & Parnell, C. E. 2002, ApJ, 572, 1048

Aschwanden, M. J. 2004, Physics of the Solar Corona,

Axford, W. I., McKenzie, J. F., Sukhorukova, G. V., Banaszkiewicz, M., Czechowski, A., & Ratkiewicz, R. 1999, Space Sci. Rev., 87, 25

Bonet, J. A., Márquez, I., Sánchez Almeida, J., Cabello, I., & Domingo, V. 2008, ApJL, 687, L131

Cirtain, J. W., et al. 2007, Science, 318, 1580

De Pontieu, B., et al. 2007, Science, 318, 1574

Erdélyi, R., & Goossens, M. 1995, A&A, 294, 575

Erdélyi, R., & Ballai, I. 2007, Astronomische Nachrichten, 328, 726

Erdélyi, R., & Fedun, V. 2007, Science, 318, 1572

Evans, C. R., & Hawley, J. F. 1988, ApJ, 332, 659

Goossens, M., Terradas, J., Andries, J., Arregui, I., & Ballester, J. L. 2009, A&A, 503, 213

Handy, B. N., et al. 1999, Sol. Phys., 187, 229

Heyvaerts, J., & Priest, E. R. 1983, A&A, 117, 220

Hollweg, J. V. 1973, ApJ, 181, 547

Hollweg, J. V. 1981, Sol. Phys., 70, 25

Hollweg, J. V. 1984, ApJ, 277, 392

Hollweg, J. V. 1986, J. Geophys. Res., 91, 4111

Hollweg, J. V., Jackson, S., & Galloway, D. 1982, Sol. Phys., 75, 35

Hudson, H. S. 1991, Sol. Phys., 133, 357

Inversity, G. W., & Priest, E. R. 1995, A&A, 302, 567

Ionson, J. A. 1978, ApJ, 226, 650

Jess, D. B., Mathioudakis, M., Erdélyi, R., Crockett, P. J., Keenan, F. P., & Christian, D. J. 2009, Science, 323, 1582

Kigure, H., & Shibata, K. 2005, ApJ, 634, 879

Klimchuk, J. A. 2006, Sol. Phys., 234, 41

Kosugi, T., et al. 2007, Sol. Phys., 243, 3

Kudoh, T., Matsumoto, R., & Shibata, K. 1998, ApJ, 508, 186

Kudoh, T., & Shibata, K. 1999, ApJ, 514, 493

Krucker, S., & Benz, A. O. 1998, ApJ, 501, L213

Liu, W., Berger, T. E., Title, A. M., & Tarbell, T. D. 2009, ApJL, 707, L37

Machida, M., & Matsumoto, R. 2003, ApJ, 585, 429

Magara, T., Mineshige, S., Yokoyama, T., & Shibata, K. 1996, ApJ, 466, 1054

Matthaeus, W. H., Zank, G. P., Oughton, S., Mullan, D. J., & Dmitruk, P. 1999, ApJL, 523, L93

McKenzie, J. F., Banaszkiewicz, M., & Axford, W. I. 1995, A&A, 303, L45

Miller, J. A. 2000, in IAU Symp. 195, Highly Energetic Physical Processes and Mechanisms for Emission from Astrophysical Plasmas, ed. P. C. H. Martens, S. Tsuruta, & M. A. Weber (San Francisco:ASP), 277

Moriyasu, S., Kudoh, T., Yokoyama, T., & Shibata, K. 2004, ApJ, 601, L107

Nishizuka, N., Shimizu, M., Nakamura, T., Otsuji, K., Okamoto, T. J., Katsukawa, Y., & Shibata, K. 2008, ApJL, 683, L83

Okamoto, T. J., et al. 2007, Science, 318, 1577

Parker, E. N. 1988, ApJ, 330, 474

Parker, E. N. 1991, ApJ, 372, 719

Parnell, C. E., & Jupp, P. E. 2000, ApJ, 529, 554

Petschek, H. E., & Thorne, R. M. 1967, ApJ, 147, 1157

Poedts, S., Goossens, M., & Kerner, W. 1989, Sol. Phys., 123, 83

Poletto, G., Vaiana, G. S., Zombeck, M. V., Krieger, A. S., & Timothy, A. F. 1975, Sol. Phys., 44, 83

Ruderman, M. S., Berghmans, D., Goossens, M., & Poedts, S. 1997, A&A, 320, 305

Saito, T., Kudoh, T., & Shibata, K. 2001, ApJ, 554, 1151

Sano, T., & Inutsuka, S. 2001, ApJ, 561, L179

Shibata, K., et al. 2007, Science, 318, 1591

Shimizu, T. 1995, PASJ, 47, 251

Shimojo, M., & Shibata, K. 1999, ApJ, 516, 934

Stone, J. M., & Norman, M. L. 1992, ApJS, 80, 791

Sturrock, P. A. 1999, ApJ, 521, 451

Suzuki, T. K. 2002, ApJ, 578, 598

Suzuki, T. K. 2004, MNRAS, 349, 1227

Takahashi, K., Nozawa, S., Matsumoto, R., Machida, M., Fukui, Y., Kudo, N., Torii, K., Yamamoto, H., & Fujishita, M., 2009, PASJ, 61, 957

Takeuchi, A., & Shibata, K. 2001, ApJ, 546, L73

Tanuma, S., Yokoyama, T., Kudoh, T., Matsumoto, R., Shibata, K., & Makishima, K. 1999, PASJ, 51, 161

Taroyan, Y., & Erdélyi, R. 2009, Space Science Reviews, 149, 229

Uchida, Y., & Kaburaki, O. 1974, Sol. Phys., 35, 451

Van Doorsselaere, T., Nakariakov, V. M., & Verwichte, E. 2008, ApJL, 676, L73

Wentzel, D. G. 1974, Sol. Phys., 39, 129

Withbroe, G. L. 1988, ApJ, 325, 442

Xiao, F., Yabe, T. & Ito, T. 1996, Comp. Phys. Comm. 93, 1

Yabe, T., & Aoki, T. 1991, Comp. Phys. Comm., 66, 219

Yokoyama, T., & Shibata, K. 1995, Nature, 375, 42

Yokoyama, T., & Shibata, K. 1997, ApJ, 474, L61

Yokoyama, T. 1998, in ESA SP-421, Proceedings of an International Meeting on Solar Jets and Coronal Plumes, (Noordwijk: ESA), 215

Table 1. Values of Parameters in Simulations

plasma $\beta$	Alfvén velocity, $v_{\rm A0}$	$R_{ m m}$
0.1	$\sim 3.5$	$\sim 2500$
1	$\sim 1.1$	$\sim 800$
20	$\sim 0.24$	$\sim 180$

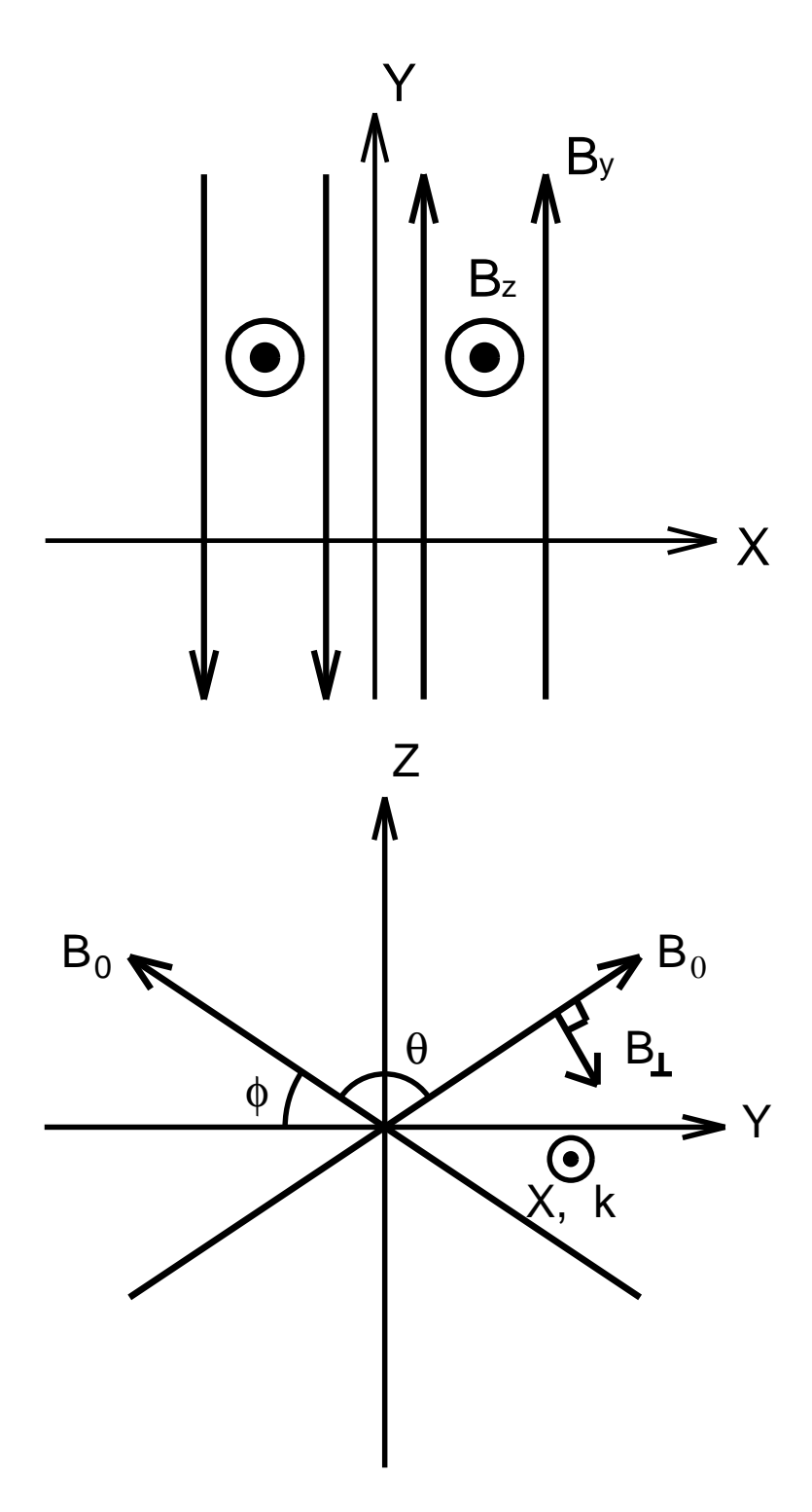


Fig. 1. Coordinate systems (xy-plane and yz-plane) of the initial magnetic field configuration in this study.

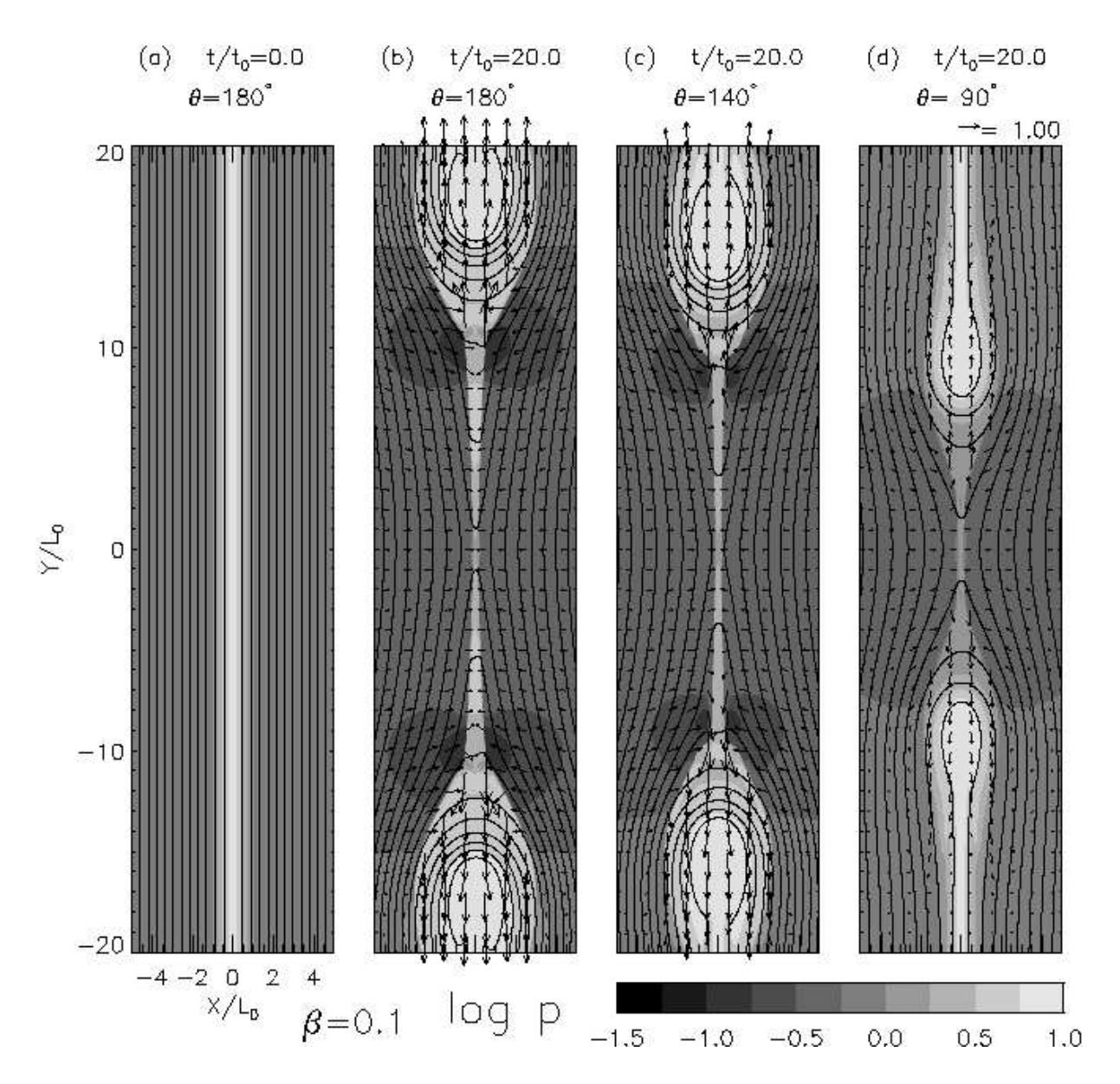


Fig. 2. Distribution of the logarithmic pressure in the case of (a)  $\theta = 180^{\circ}$  at initial state, (b)  $\theta = 180^{\circ}$  at  $t/t_0 = 20.0$ , (c)  $\theta = 140^{\circ}$  at  $t/t_0 = 20.0$  and (d)  $\theta = 90^{\circ}$  at  $t/t_0 = 20.0$ . The plasma  $\beta$  is 0.1. The black lines show the magnetic field lines, and the arrows show the velocity.

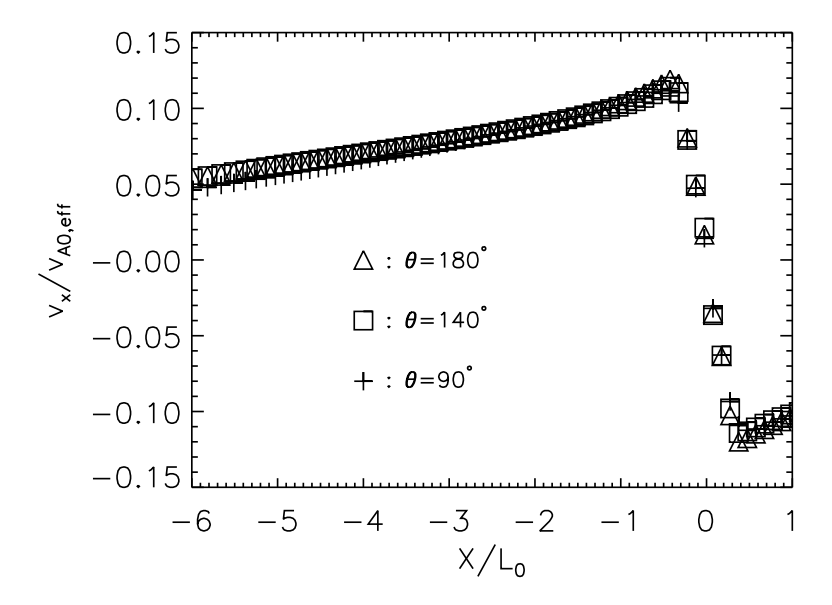


Fig. 3. The distribution of the x-component of the velocity normalized by  $v_{A0}\cos(90^{\circ}-\theta/2)=v_{A0,eff}$  on a line where y=0 at  $t/t_0=20$ . The triangles display the results of the  $\theta=180^{\circ}$  case, the squares display the results of the  $\theta=140^{\circ}$  case, and the plus signs display the results of the  $\theta=90^{\circ}$  case. The plasma  $\beta$  is 0.1. The inflow velocities,  $v_x$  in this case, are roughly proportional to  $\cos(90^{\circ}-\theta/2)$ . This can be interpreted as  $v_x \propto v_{A0,eff}$ , where  $v_{A0,eff}$  is the Alfvén velocity in the computational plane.

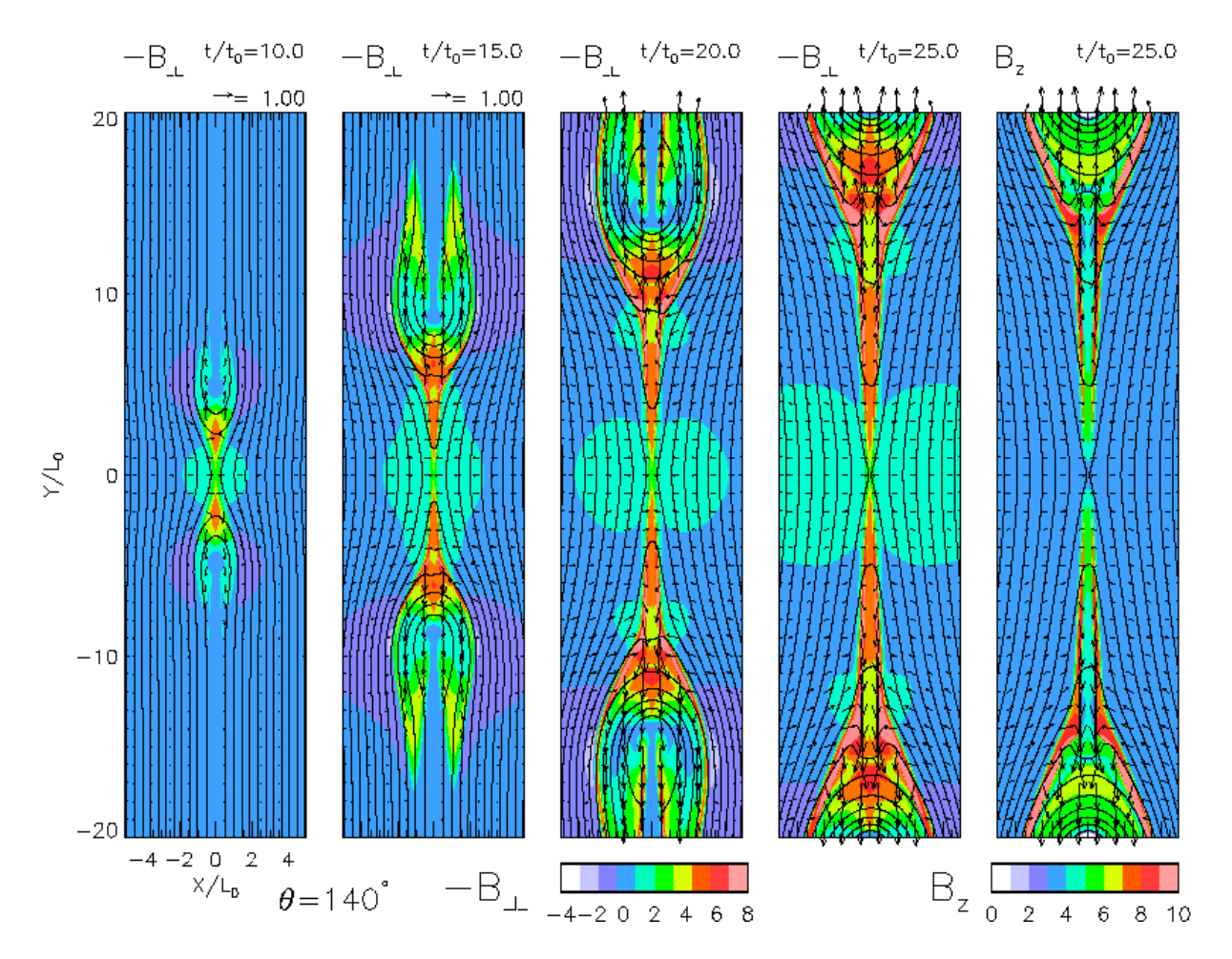


Fig. 4. The left four panels show the time evolution of the magnetic field component perpendicular to the initial field,  $-B_{\perp}$ , in the case of  $\theta = 140^{\circ}$ . The right panel shows the  $B_z$  distribution at  $t/t_0 = 25$ . The plasma  $\beta$  is 0.1. The black lines show the magnetic field lines, and the arrows show the velocity.

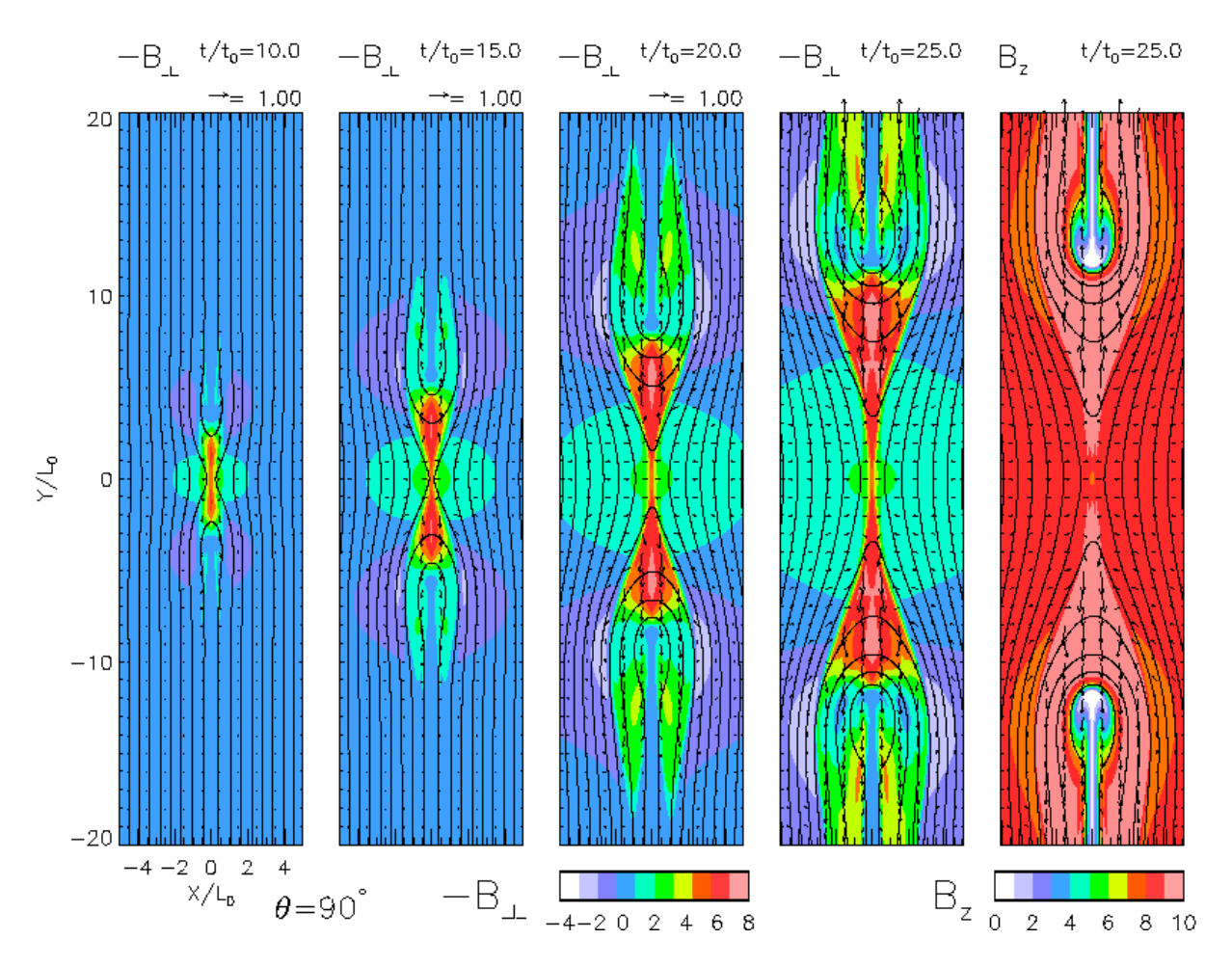


Fig. 5. The left four panels show the time evolution of the magnetic field component perpendicular to the initial field,  $-B_{\perp}$ , in the case of  $\theta = 90^{\circ}$ . The right panel shows the  $B_z$  distribution at  $t/t_0 = 25$ . The plasma  $\beta$  is 0.1. The black lines show the magnetic field lines, and the arrows show the velocity.

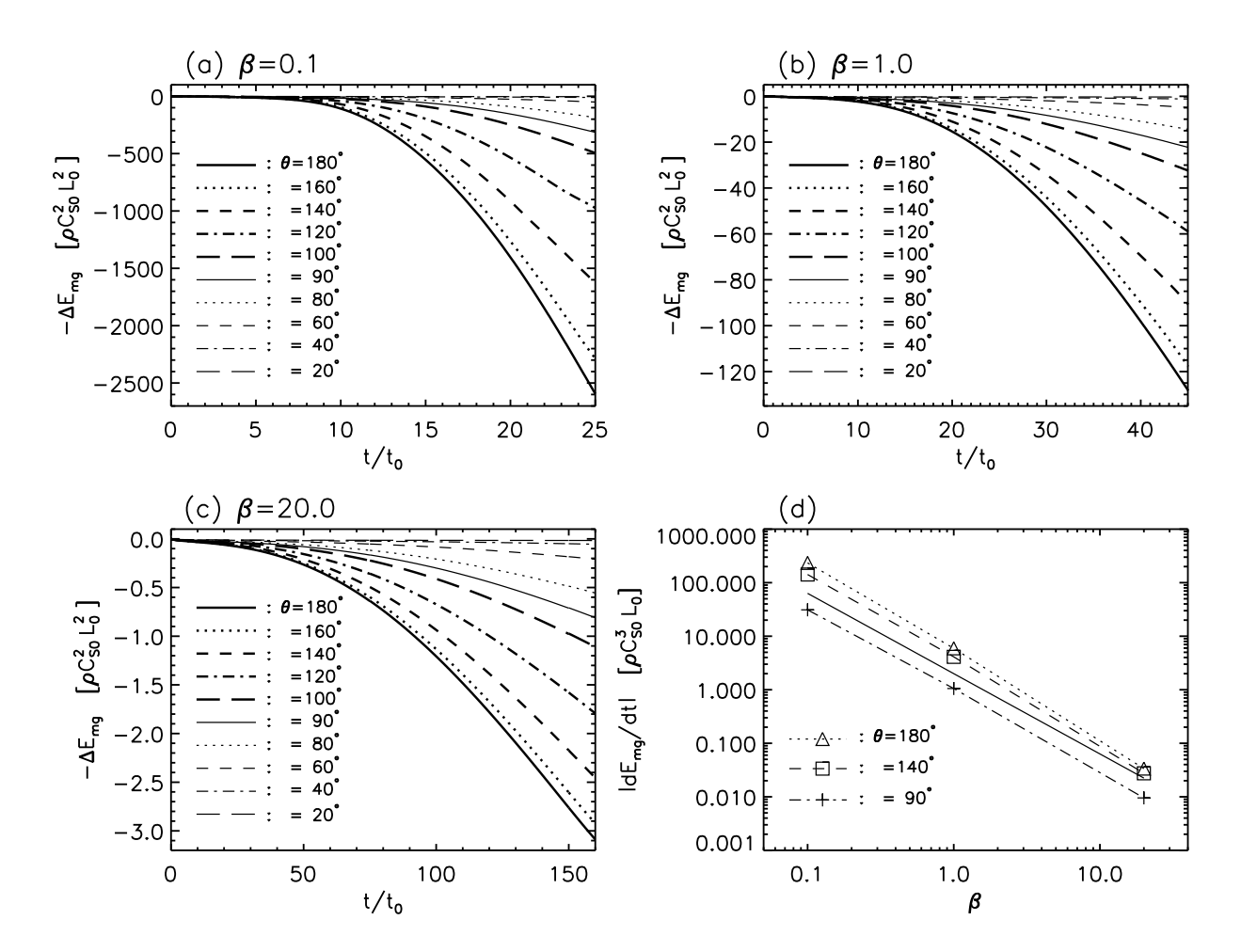
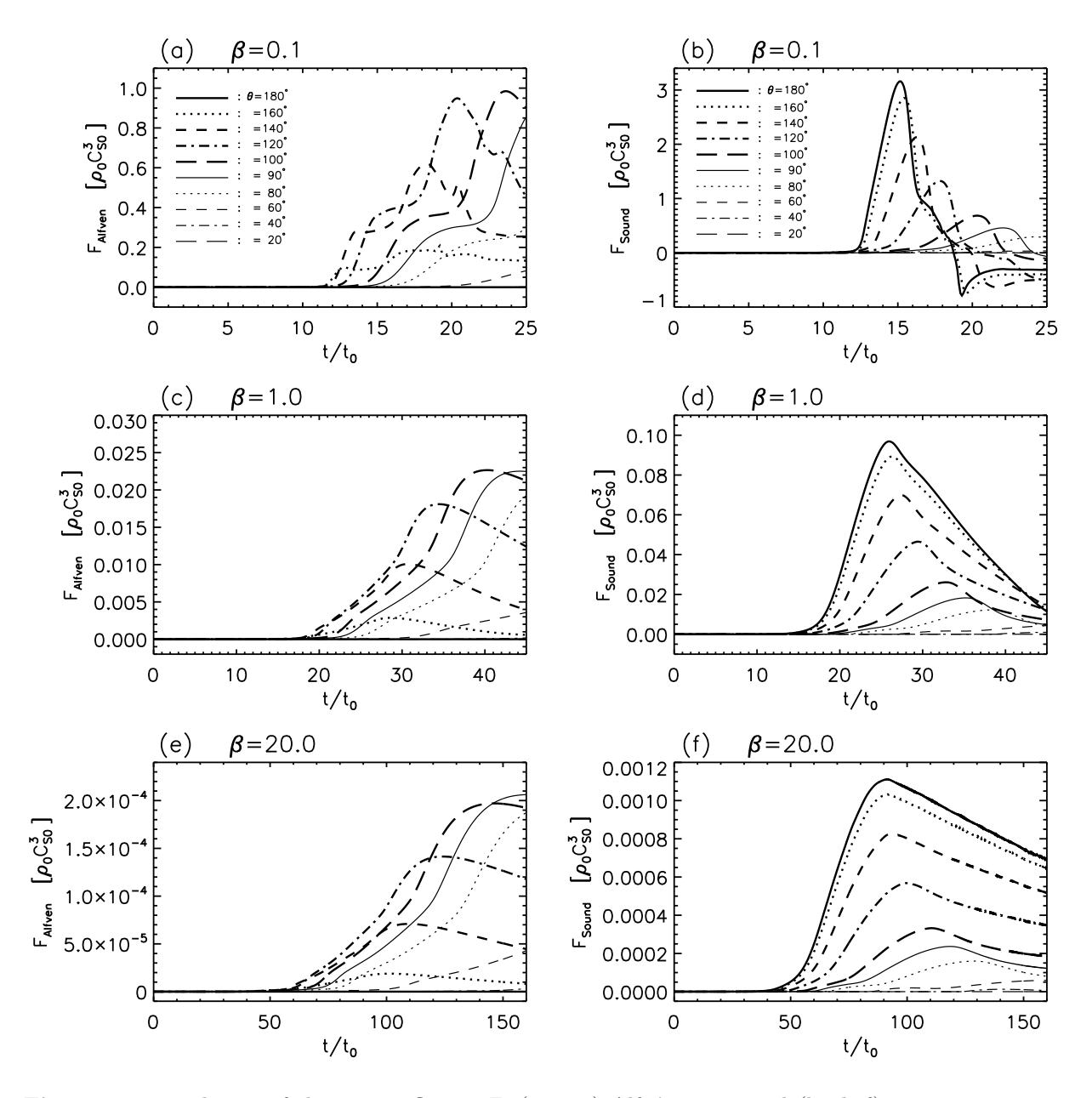


Fig. 6. (a)-(c) Time evolution of the released magnetic energy in the computational domain in each  $\theta$  case. The plasma  $\beta$  are (a) 0.1, (b) 1, and (c) 20. (d) The dependence of the magnetic energy release rate in the late stage on  $\beta$  in each  $\theta$  case. The solid line shows a line where  $|dE_{\rm mg}/dt| \propto \beta^{-3/2}$ . The magnetic energy release rate is proportional to  $\beta^{-3/2}$ , which is consistent with the theoretical prediction, independent of  $\theta$ .



**Fig. 7.** Time evolution of the energy fluxes, F, (a, c, e) Alfvén waves and (b, d, f) magneto-acoustic waves in each  $\theta$  case. The plasma  $\beta$  are (a, b) 0.1, (c, d) 1.0 and (e, f) 20.0.

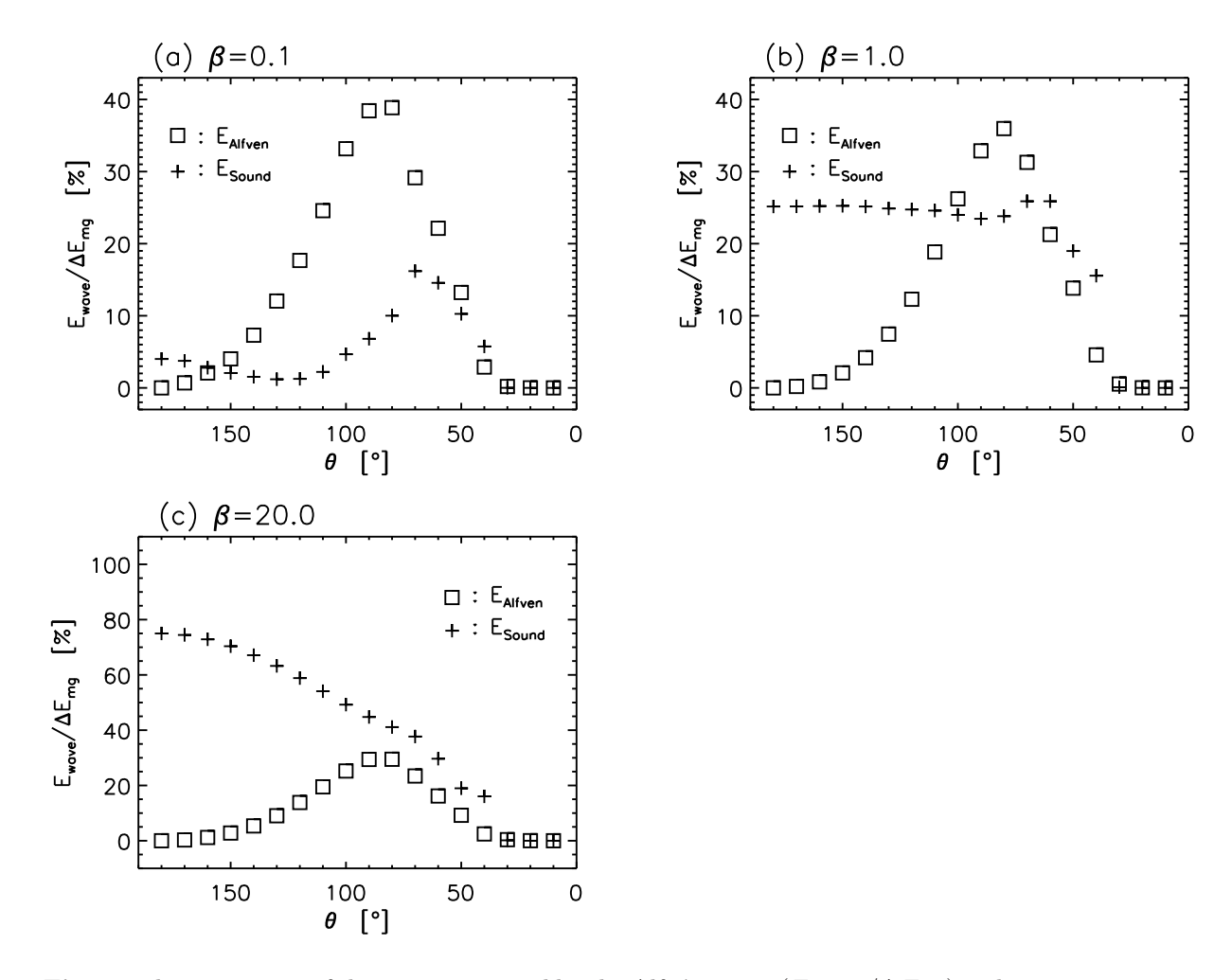


Fig. 8. The percentage of the energies carried by the Alfvén waves  $(E_{\rm Alfven}/\Delta E_{\rm mg})$  and magneto-acoustic waves  $(E_{\rm Sound}/\Delta E_{\rm mg})$  to the released magnetic energy at the final stage of simulation in the case of  $\theta = 180^{\circ}$ .

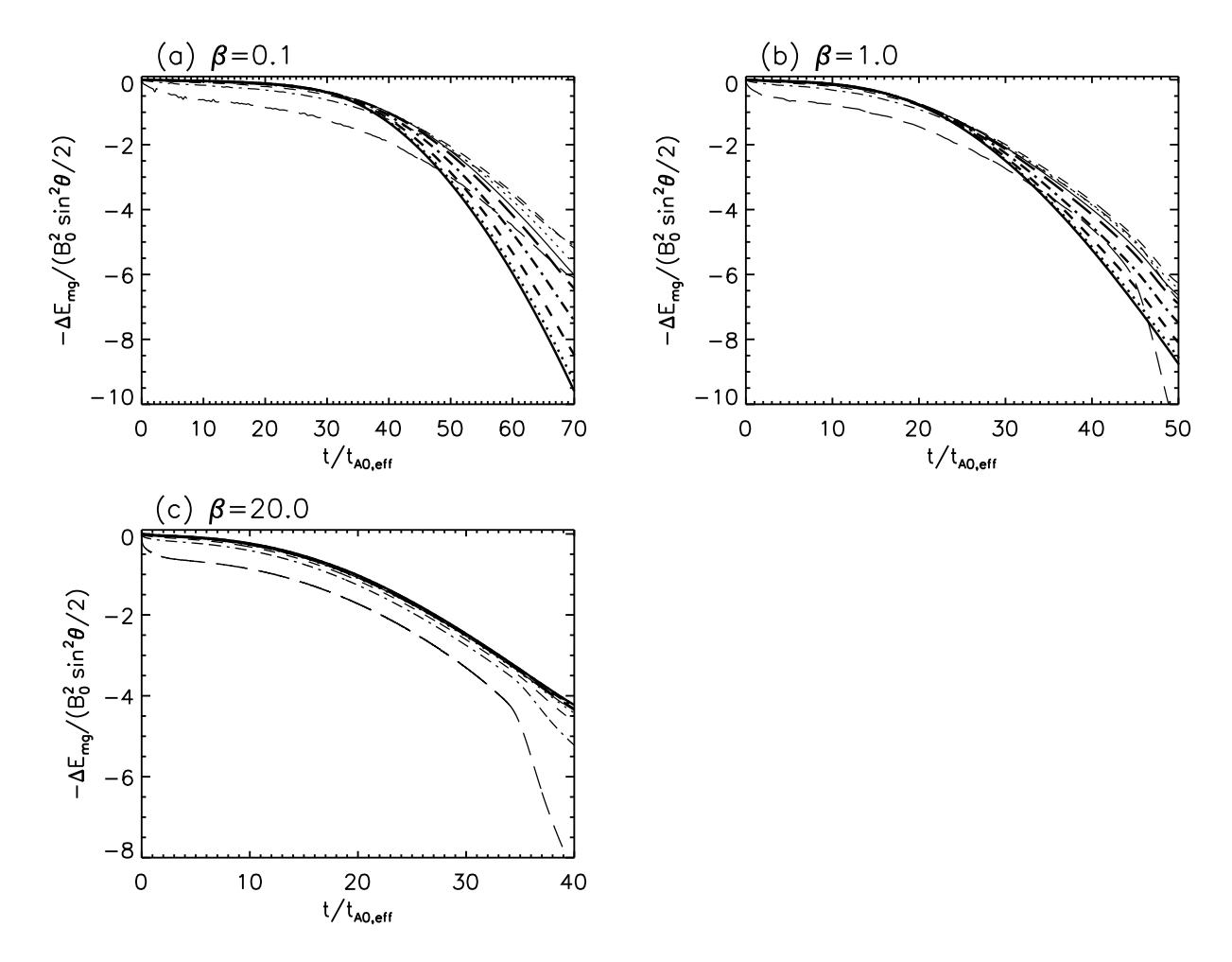


Fig. 9. Time evolution of the magnetic energy in the computational domain in each  $\theta$  case. Compared with Figure 6, the horizontal axis, time, is re-normalized by the effective Alfvén time  $(t_{\rm A0,eff}=L_0/v_{\rm A0,eff})$ . The vertical axis, the difference of the magnetic energy from the initial value, is also re-normalized as  $-\Delta E_{\rm mg}^* = -\Delta E_{\rm mg}/(B_0^2 \sin^2 \theta/2)$ . The line styles are the same as Figure 6.

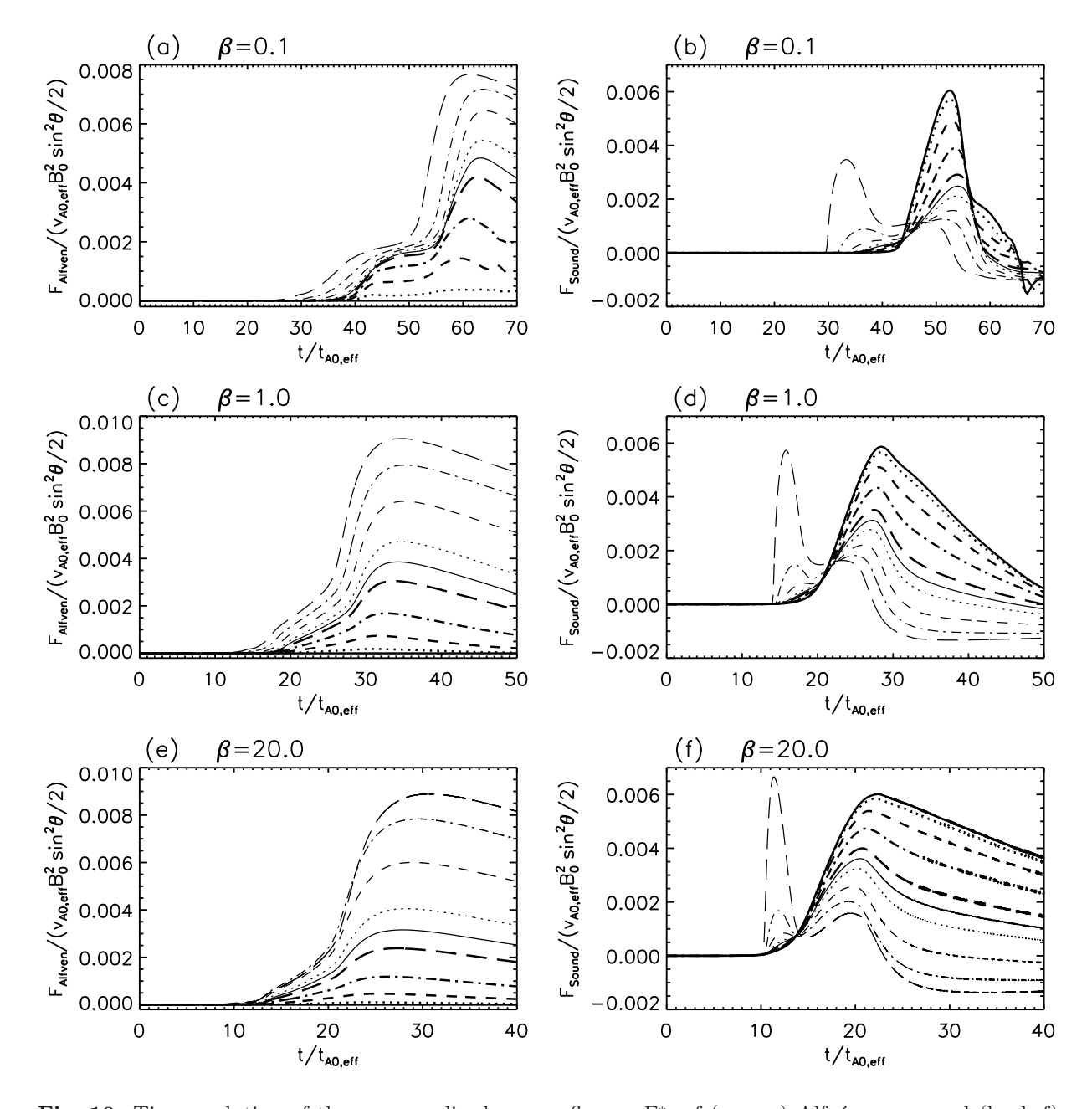


Fig. 10. Time evolution of the re-normalized energy fluxes,  $F^*$ , of (a, c, e) Alfvén waves and (b, d, f) magneto-acoustic waves in each  $\theta$  case. The energy fluxes are re-normalized as  $F^* = F/(v_{A0,eff}B_0^2\sin^2\theta/2)$ . The plasma  $\beta$  are (a, b) 0.1, (c, d) 1.0 and (e, f) 20.0. The line styles are the same as Figure 7.

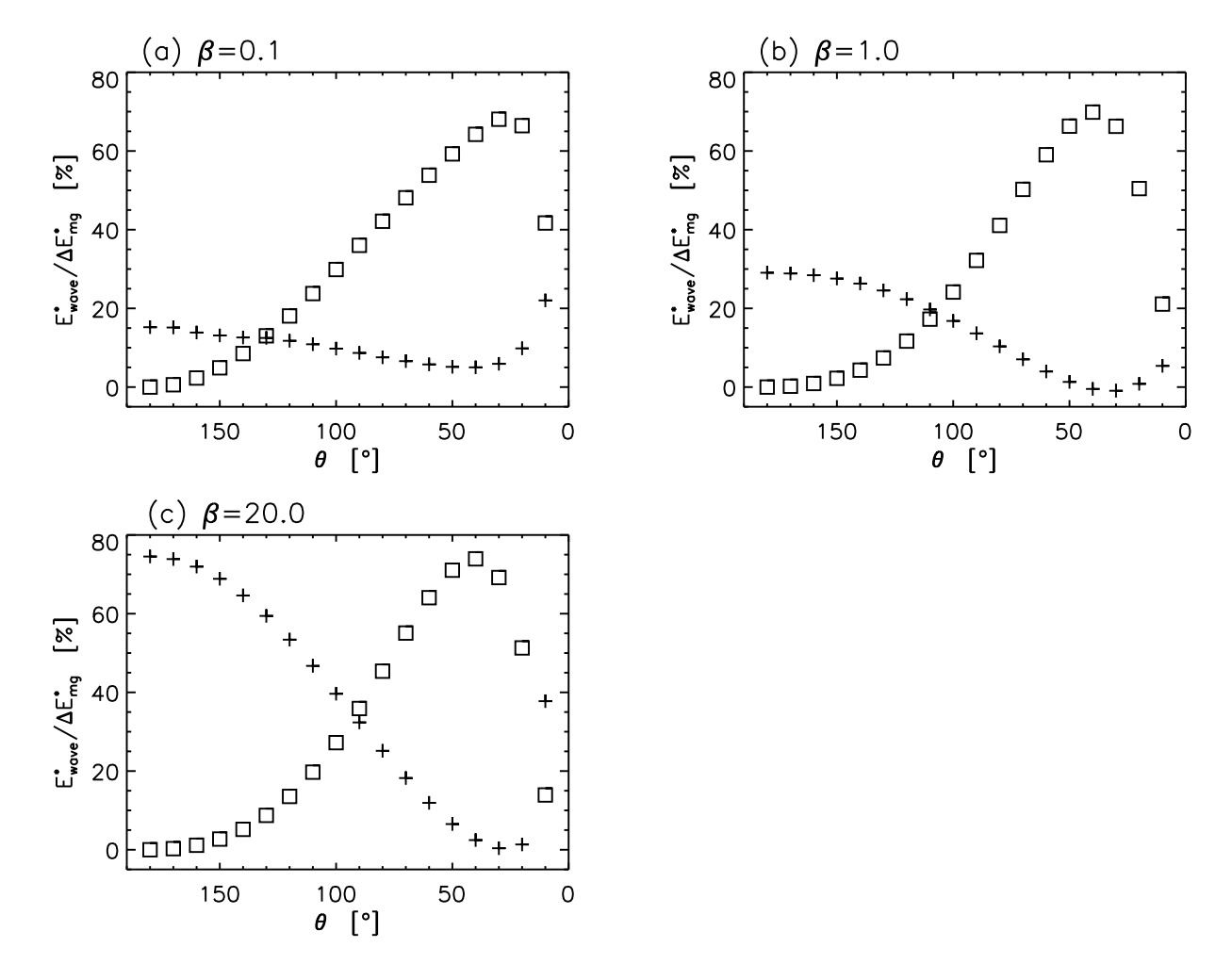


Fig. 11. The percentage of the energies carried by the Alfvén waves  $(E_{\rm Alfven}^*/\Delta E_{\rm mg}^*)$  and magneto-acoustic waves  $(E_{\rm Sound}^*/\Delta E_{\rm mg}^*)$  to the released magnetic energy. The released magnetic energy is re-normalized by the energy of the initial magnetic field which can reconnect. The symbols are the same as Figure 8.